SCIENCE CHINA
Information Sciences

• REVIEW •

August 2018, Vol. 61 080401:1–080401:13
https://doi.org/10.1007/s11432-017-9361-3

Special Focus on Photonic Devices and Integration

Hybrid-cavity semiconductor lasers with a whispering-gallery cavity for controlling Q factor

Yongzhen HUANG*, Xiuwen MA, Yuede YANG, Jinlong XIAO & Yun DU

State Key Laboratory on Integrated Optoelectronics, Institute of Semiconductors & College of Materials Science and Optoelectronic Technology, University of Chinese Academy of Sciences, Chinese Academy of Sciences, Beijing 100083*, China*

Received 28 November 2017/Revised 13 January 2018/Accepted 6 February 2018/Published online 18 May 2018

Abstract Hybrid cavities composed of a Fabry-Pérot (FP) cavity and a whispering-gallery mode (WGM) microcavity have been proposed and demonstrated for modulating mode Q factor to realize single mode and optical bistable lasers. In this article, we report hybrid cavity lasers with a pentagon microcavity and a square microcavity, respectively. The reflectivity spectra of different microcavities are simulated to select microcavities for hybrid cavities. Mode coupling with mode Q factor enhancement is investigated numerically and experimentally. Stable single mode operations with a high coupling efficiency to a single mode fiber are realized for a hybrid cavity laser with a square microcavity. Furthermore, optical bistability hybrid lasers are investigated as the microcavity is unbiased, due to saturable absorption in the microcavity and mode competition, respectively. All-optical flip-flop is demonstrated using trigger optical pulses with a width of 100 ps for mode competition bistability. The stable single mode operation and optical bistability of hybrid cavity lasers may shed light on the applications for photonic integrated circuits and optical signal processing.

Keywords optical microcavity, semiconductor lasers, hybrid cavity, optical bistability, single mode laser

Citation Huang Y Z, Ma X W, Yang Y D, et al. Hybrid-cavity semiconductor lasers with a whispering-gallery cavity for controlling Q factor. Sci China Inf Sci, 2018, 61(8): 080401, https://doi.org/10.1007/s11432-017-9361-3

1 Introduction

Whispering-gallery mode (WGM) microcavities have been extensively studied for applications in microlasers for near three decades [1–5]. In addition to microdisk and deformed microdisks, polygonal microcavities can also support high-Q WGMs for realizing directional emission microlasers [6–10]. Due to short cavity length, it is easy to realize single longitudinal mode operation for microcavity lasers. However, a conventional Fabry-Pérot (FP) cavity laser with a cavity length of 200–300 µm is usually multiple longitudinal lasing. Recently, a novel hybrid cavity composed of an FP cavity and a square microcavity has been demonstrated for mode selection by enhancing mode Q factor for hybrid mode between WGM and FP mode. The mode Q factor enhancements are numerically and experimentally demonstrated for the hybrid modes with a mode wavelength interval of microcvaviy longitudinal mode interval. Stable single-mode operation with high coupling efficiency to a single mode fiber is realized by injecting currents to the square microcavity and the FP cavity sections at the same time [11–13].

Different coupled cavities, such as cleaved coupled-cavity lasers, V-coupled cavities, coupled rings, and multimode interference coupler have been investigated to realizing single mode semiconductor lasers for

---

* Corresponding author (email: yzhuang@semi.ac.cn)

the past decades [14–19]. In addition, mode couplings of nanocavities or between a nanocavity and a waveguide have been studied for dynamical control of Q factor [20–25]. Tuning Q factor via frequency shift for an ultra-high Q cavity was employed to release trapped light and generate a short pulse [22]. Strong mode coupling between a nanocavity and a long multimode cavity was demonstrated based on the level anticrossing [24], and the spontaneous emission waveform was controlled for coupled photonic crystal cavities [25].

Compared to cleaved coupled-cavity lasers, which is a coupled cavity composed of two FP cavities with a small gap, the hybrid cavity of a square microcavity and an FP cavity can reach much stable single mode operation over a wide injection current range [11, 12]. Furthermore, controllable optical bistability is realized due to mode competition as the square microcavity is unbiased, and all-optical set and reset operations are demonstrated [26]. Various geometries of bistable laser diodes have been demonstrated [27–33], with the advantages in optical gain and low optical switching energy for optical signal processing. Photonic crystal nanolasers were demonstrated as an all-optical random-access memory with error-free flip-flop operation at 5 Gb/s [34, 35]. Optical bistability based on mode competition can avoid the optical switching time limit of carrier lifetime. Optical memories using competition of counter-propagation modes in coupled-ring and microdisk lasers [29,32] were achieved, but which require extremely smooth resonator sidewalls to avoid the mode reflection. In addition, optical switchings between different polarization modes were investigated using GaAs and InP based vertical cavity surface-emitting lasers (VCSELs) [36–38]. However, VCSELs are not suitable for on-chip planar integration circuits.

In this paper, we summarize the characteristics of hybrid cavity lasers with a WGM resonator for realizing mode selection due to mode coupling. In Section 2, we simulate reflectivity spectra for different WGM microcavities, as one side reflector for the FP cavity of the hybrid cavity. Hybrid mode behaviors for whole hybrid cavity are discussed by calculating the mode wavelengths and mode Q factors. The fabrication technique processes are simply summarized in Section 3. In Section 4, lasing characteristics are investigated for a hybrid cavity laser with a pentagon microcavity. In Section 5, the output characteristics are presented for a hybrid cavity laser with a square microcavity. In Section 6, optical bistability with all-optical flip-flop is discussed for a hybrid cavity laser with a square microcavity, and conclusion is presented in Section 7.

2 Simulation for hybrid cavities

The hybrid cavities have high Q coupled modes between WGMs and FP modes, and the high Q coupled modes with a large wavelength interval are easy to realize stable single mode operation [11, 12]. In this section, a two-dimensional (2D) finite-difference time-domain (FDTD) method is first utilized to calculate the mode reflectivity spectra of different microcavities, for the fundamental mode of the FP cavity as it impinges the interface between the WGM microcavity and the FP cavity. The reflectivity spectra are approximately calculated as the reflected/incident intensity spectra ratio $|E_r|^2/|E_i|^2$ [11,12], where E_i and E_r are input and reflected field amplitudes at the midpoint of the FP waveguide. Taking the fundamental FP waveguide mode exciting source with a time domain profile as $P(t) = \exp[-(t-t_0)^2/t_w^2]\cos(2\pi f_0 t)$ with $t_w = 1.195$ fs, $t_0 = 3t_w$, and $f_0 = 193.5$ THz, we calculate the reflectivity spectra for transverse-electric (TE) mode by the Padé approximation [39] using the input and reflected fields at a distance of 18 μm away from the center of the microcavity. The microcavities with a refractive index of 3.2 are confined by a bisbenzo cyclobutene (BCB) layer with a refractive index of 1.54.

The reflectivity spectra for an FP cavity end face, a microdisk, a square microcavity and a pentagon microcavity are calculated and plotted in Figure 1 with the FP cavity width $d = 0.4$ μm and the gain $g = 0$. The reflectivity is about 0.10 for the FP cavity end face as shown in Figure 1(a), which is 20% smaller than the reflectivity determined by the refractive index difference for a vertical propagating plane wave. For a microdisk cavity with a radius of 5 μm, we have a lot of narrow reflectivity peaks as shown in Figure 1(b), corresponding to high Q coupled WGMs in the microdisk connecting with a waveguide [40]. The reflectivity spectra show a series of wide peaks for a square microcavity with a

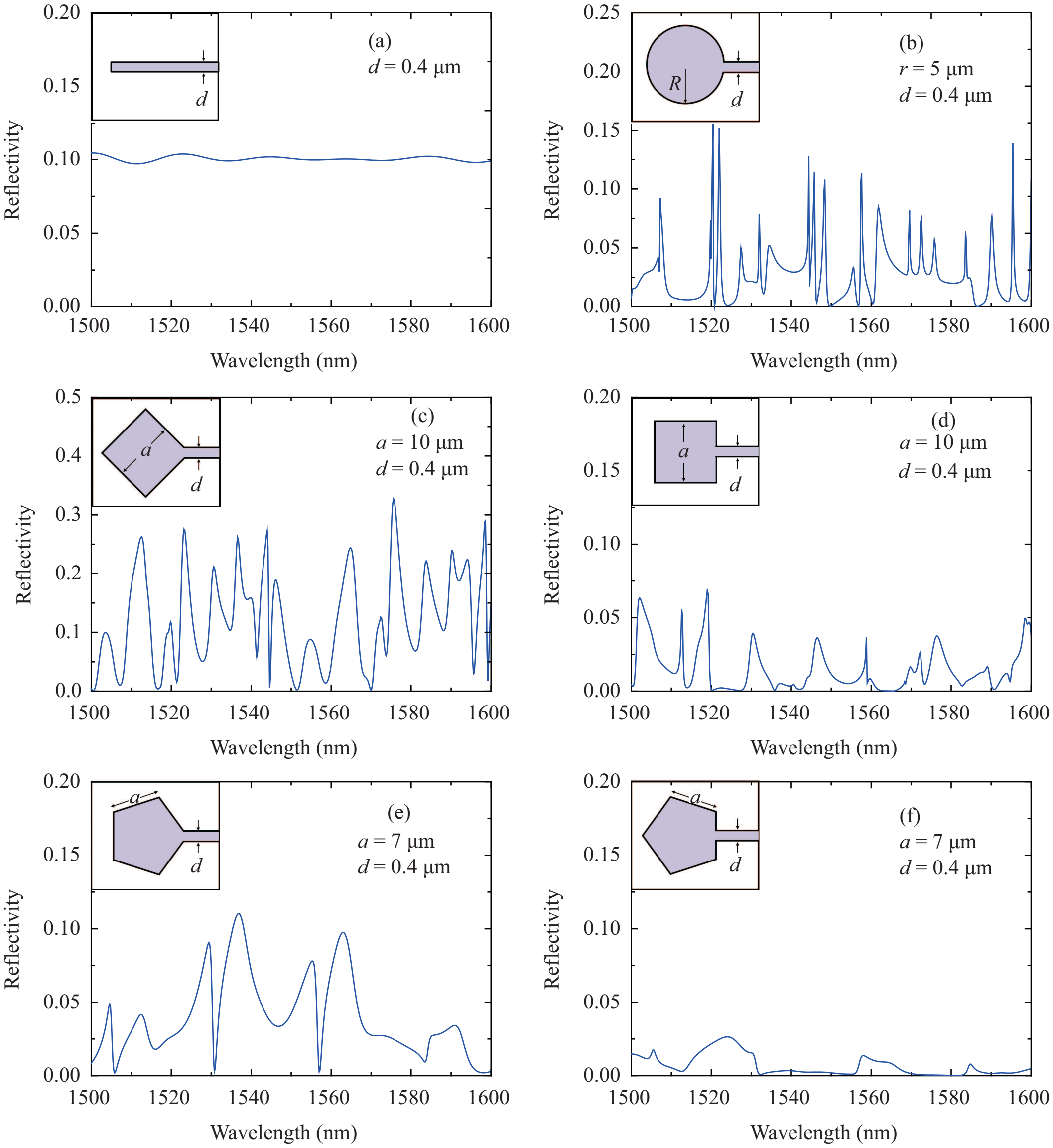

Figure 1 (Color online) Simulated reflectivity spectra for (a) an FP end face with a width $d = 0.4$ μm, (b) a microdisk cavity with a radius of $r = 5$ μm, (c) a vertex and (d) the middle point of one side of a square microcavity with a side length $a = 10$ μm, and (e) a vertex and (f) the middle point of one side of a pentagon microcavity with a side length $a = 7$ μm.

side length of 10 μm as shown in Figure 1(c) and (d), which shows much higher reflectivity peaks as the FP cavity connected to a vertex of the square resonator. For a pentagon microcavity with a side length of 7 μm, less and lower reflectivity peaks than the square microcavity are obtained as shown in Figure 1(e) and (f). In addition, we also calculate the reflectivity for an equilateral triangle resonator with a side length of 14 μm, and obtain the reflectivity about 0.01. The results indicate that square microcavity can have much higher resonant reflectivity peaks than the other WGM microcavities. To avoid the influence of the high order transverse mode on the approximation method by using the field amplitudes at the midpoint of the FP waveguide, we choose a narrow FP cavity for calculating mode reflectivity in the above simulation. However, such narrow waveguide cannot be fabricated by contact photolithography technique. In the following part, we simulate mode characteristics for hybrid cavities with an FP waveguide width of 1.5 μm.

The TE mode characteristics are simulated for a 2D hybrid cavity with a square microcavity in the x-y plane. The mode wavelengths and Q factors of even symmetric mode of the FP cavity are calculated from

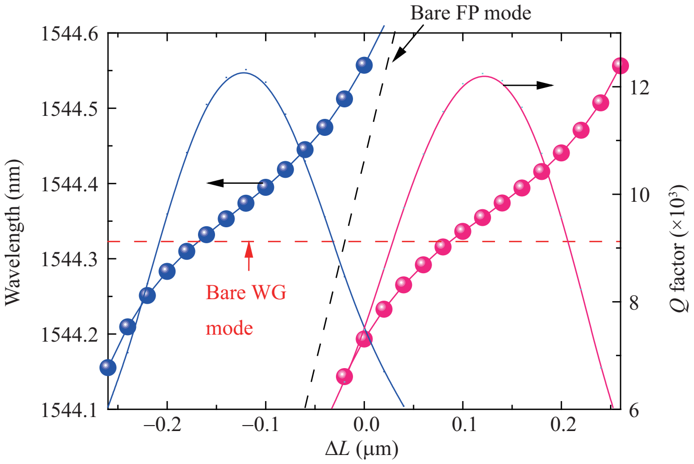

Figure 2 (Color online) Mode wavelength and Q factor versus the variation in L for even WG-FP hybrid modes in a square-FP hybrid cavity with a = 10 μm, d= 1.5 μm and L = 300 μm.

solved complex eigen frequencies. The mode wavelengths and Q factors versus the variation of FP cavity length ΔL are plotted in Figure 2 for a hybrid cavity with a square cavity side length a = 10 μm, FP length and width L = 300 μm and d= 1.5 μm. The red horizontal dashed line at 1544.32 nm is the mode wavelength of the bare WG fundamental mode with the Q factor of 7.39 × 10^3 in the square cavity. The black dashed line is the mode wavelength of a longitudinal mode versus L, as the fundamental transverse mode in the bare FP cavity. The variation of mode wavelength shows strong mode coupling around the crossing point between the bare WGM and FP mode. Similar mode coupling is obtained by varying the refractive index of the FP cavity [11, 12].

We also simulate a hybrid cavity with a square side length a = 15 μm, and FP cavity width and length d = 1.5 μm and L = 300 μm. The obtained mode Q factors as the functions of the mode wavelengths are plotted in Figure 3(a) at the square resonator gain g_{SQ}= 0 and 4 cm^{-1}. Two high Q modes with Q factors of 1.3×10^4 and 1.14×10^4 are observed at wavelengths of 1531.73 nm and 1567.02 nm as g_{SQ}= 0, with a free spectral range (FSR) of 35.29 nm, which is twice the longitudinal mode intervals for the symmetric mode relative to the diagonal of the square [6]. At g_{SQ}= 4 cm^{-1}, the Q factors becomes 2.03×10^4 and 1.64×10^4 as shown in Figure 3(a). The mode intensity distributions of squared magnetic field $|H_z|^2$ are plotted in Figure 3(b) for the high-Q TE mode at 1531.73 nm in the square microcavity and the output facet of the FP cavity, with the mode intensity in the FP cavity is magnified by 10 times for clarify. The mode distribution is corresponding to symmetric modes in the square cavity as well as the FP cavity, but contains higher order transverse mode field component in addition to the fundamental transverse mode of the FP cavity, i.e., the hybrid mode is not a pure fundamental transverse mode in the FP cavity. Comparing different mode field distributions, we conclude that the high Q mode has strong mode field distribution in the square microcavity [11, 12].

3 Fabrication of hybrid cavity lasers

Based on the above simulation, we choose to fabricate hybrid cavity lasers with a square or pentagon microcavity due to higher reflectivity or less number of resonance reflectivity peaks. Hybrid cavity lasers are fabricated using an AlGaInAs/InP laser wafer with eight compressively strained quantum wells. The total thickness of upper p-InP cladding layer and p$^+$-InGaAs contact layer is 1.6 μm. Contact photolithography and inductively coupled plasma (ICP) etching techniques are applied to fabricate hybrid cavity lasers with an etching depth of about 4 μm. Then a 200-nm SiN$_x$ layer is deposited and a BCB confinement layer is applied to form a planar surface. An isolation trench region is formed by etching off p$^+$-InGaAs contact layer between the FP cavity and the microcavity, and p-electrodes are patterned by metal deposition and lift-off processes. Figure 4(a) shows the scanning electron microscope (SEM) image

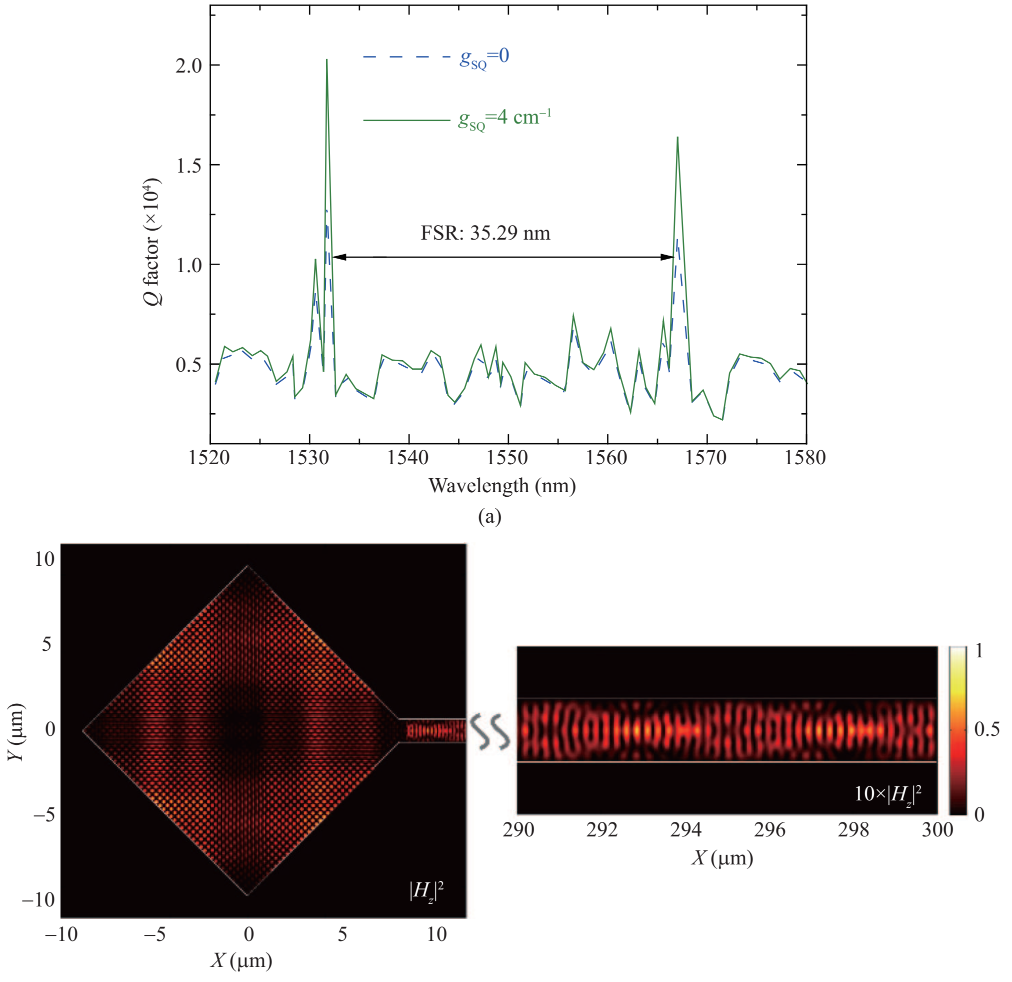

(a)

(b)

Figure 3 (Color online) (a) Calculated mode Q factor versus mode wavelength at $g_{\mathrm{SQ}} = 0$ and 4 cm^{-1} for a hybrid cavity with a square resonator at $a = 15$ μm, $d = 1.5$ μm, and $L = 300$ μm. (b) Mode intensity distributions of $|H_z|^2$ in the square and FP sections for the high Q mode of 1531.73 nm at $g_{\mathrm{SQ}} = 0$. The mode intensity in the FP section is magnified by 10 times for clarify.

of the isolation trench region after depositing p-electrode and the lift-off process, where an unneeded additional groove is formed due to a wide photomask than the waveguide. Figure 4(b) is a SEM image of the cross section of cleaved FP cavity after BCB planarization process. Microscopic image in Figure 4(c) shows a fabricated hybrid cavity laser with a pentagon microcavity after the deposition of p-type and n-type electrodes. Two patterned p-type electrodes are used for microcavity and FP cavity separately. Figure 4(d) is a microscopic image of a hybrid cavity laser with a square microcavity.

4 Hybrid cavity laser with a pentagon microcavity

After cleaving over the FP cavity, the hybrid cavity lasers are tested by mounting on an AlN submount with the temperature controlled by a thermoelectric cooler (TEC). The lasing characteristics are first reported for a hybrid cavity laser with a pentagon microcavity at a side length of 10 μm, and FP cavity width $d = 1.5$ μm and length $L = 300$ μm. The output powers coupled into a tapered single-mode fiber (SMF) are plotted in Figure 5(a) versus increased continuous-wave (CW) FP-cavity current I_{FP}, at pentagon-cavity injection current $I_{\mathrm{PE}} = 0$, 1, and 2 mA, respectively. Based on output power-current curves, lasing threshold currents of 38, 18, and 17 mA are estimated for the laser at $I_{\mathrm{PE}} = 0$, 1, and 2 mA, respectively, and the corresponding maximum output powers are 0.87, 1.04, and 1.05 mW.

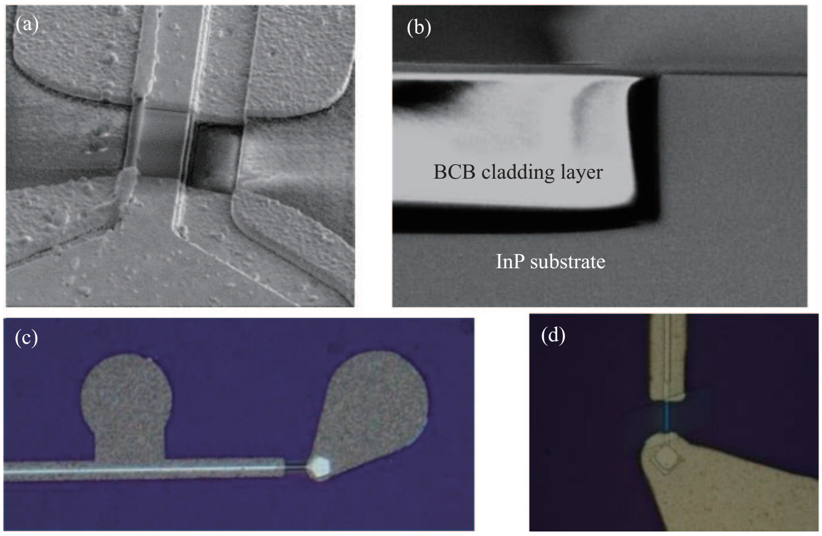

Figure 4 (Color online) SEM images of (a) an isolation trench region and (b) cleaved FP cavity after BCB planarization process. Microscopic images of hybrid cavity lasers with (c) a pentagon microcavity and (d) a square microcavity.

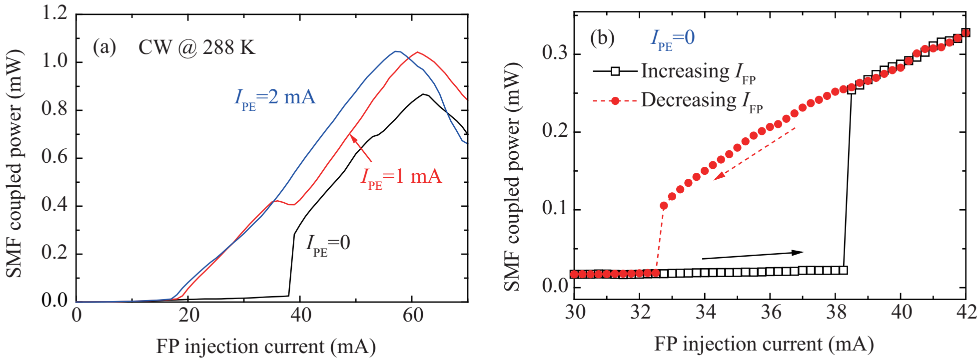

Figure 5 (Color online) (a) SMF coupled power versus increased FP-cavity current $I_{\rm FP}$ at $I_{\rm PE}=0$, 1, and 2 mA, respectively, and (b) SMF coupled power measure by increasing and decreasing $I_{\rm FP}$ at $I_{\rm PE}=0$, for a pentagon-cavity current for a pentagon-FP laser with $a=10$ μm, $W=1.5$ μm, and $L=300$ μm.

Decreased lasing threshold and improved output power are obtained with the increase of the pentagon cavity pump level. Note that a sudden increase in the output power occurs around the threshold at $I_{\rm PE}=0$, so we measure the output power by increasing and decreasing the FP-cavity injection current $I_{\rm FP}$ at $I_{\rm PE}=0$, respectively, with a time step of 1 s by varying $I_{\rm FP}$ at an interval of 0.25 mA. As shown in Figure 5(b), an anticlockwise bistable hysteresis loop is observed as $I_{\rm FP}$ varies between 32 and 39 mA. The output powers at $I_{\rm FP}=38$ mA are 0.25 and 0.022 mW for the upper and lower states, respectively, with a ratio of 11 dB. The optical bistability could be attributed to absorption saturation in the pentagon microcavity owing to the accumulation of photon generated carriers as in [41, 42], as the lasing mode is absorbed in the microcavity section to generate carriers. However, the optical bistability due to the saturable absorption usually cannot be switched off by an optical signal pulse and switching time is limited by carrier lifetime. The results show that the variation of the pentagon cavity pump level would greatly influence the equivalent reflectivity of the hybrid laser. In fact, the microcavity can also work as a modulator to modulate the hybrid cavity laser output power. The decrease of output power as $I_{\rm FP}>60$ mA is mainly caused by the increase of the laser cavity temperature and related mode jumping. Although the TEC temperature keeps near a constant, the laser cavity temperature still increases with the injection current greatly.

The lasing spectra of the hybrid cavity laser are plotted in Figure 6(a) and (b) at $I_{\rm FP}=40$ mA and $I_{\rm PE}=2$ mA, and Figure 6(c) at $I_{\rm PE}=1$ mA and $I_{\rm FP}$= 30, 36, and 43 mA. Single mode operation at

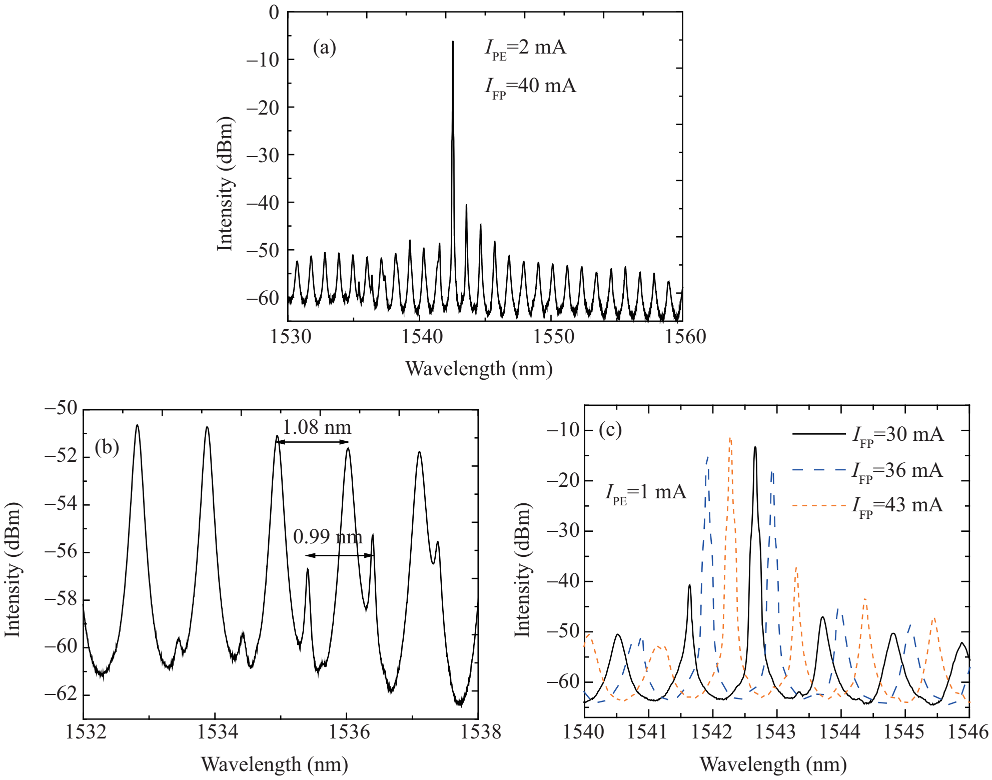

Figure 6 (Color online) Lasing spectra for the hybrid cavity laser with pentagon microcavity side length a = 10 μm, and FP cavity width d = 1.5 μm and length L = 300 μm, (a) and (b) at $I_{\rm FP}$ = 40 mA and $I_{\rm PE}$ = 2 mA, and (c) at $I_{\rm PE}$ = 1 mA and $I_{\rm FP}$= 30, 36, and 43 mA.

1542.54 nm is realized with a side-mode suppression ratio (SMSR) of 34 dB in Figure 6(a). In addition, minor peaks are observed in two sides of the lasing peaks around 1535 and 1544 nm, respectively. The detail spectra around 1535 nm are magnified in Figure 6(b) with evident minor resonance peaks at a wavelength interval of 0.99 nm compared to an interval of 1.08 nm for the major peaks. However, the minor peaks have narrower width than that of the major peaks in Figure 6(b), which indicates higher Q factor for the minor modes. The minor peaks may be the higher order transverse mode of the FP cavity. With the increase of $I_{\rm FP}$, the lasing mode shifts to longer wavelength and jumps from 1543.81 to 1558.04 nm at $I_{\rm FP}$ = 60 mA with a wavelength interval of 14.23 nm determined by the resonance of the pentagon microcavity. A resonance mode wavelength shifts 2.62 nm as $I_{\rm FP}$ increases from 20 to 70 mA due to the heating effect, which corresponding a temperature rise of about 26 K.

5 Hybrid cavity laser with a square microcavity

For a hybrid cavity laser with a square microcavity at side length a = 10 μm, and an FP cavity with d = 1.5 μm and L = 300 μm, the output powers coupled into a SMF as functions of FP cavity injection current are plotted in Figure 7, with threshold current of 16, 12, and 10 mA, respectively, as the square cavity injection current $I_{\rm SQ}$ = 1, 5 and 10 mA. The output power is 2.5 mW at $I_{\rm FP}$ = 60 mA and $I_{\rm SQ}$ = 10 mA. In addition, we obtain near equal output powers by coupling into a multiple mode fiber and the SMF as the FP cavity injection current is less than 60 mA for the laser, i.e., before the mode jumping, which imply a high coupling efficiency to a SMF. Coupling efficiency as high as 50% to a SMF was obtained for a hybrid laser in [11]. Furthermore, we obtain near circular far-field pattern by measuring output power versus the position of the SMF in horizontal and vertical directions.

Lasing spectra of the hybrid cavity laser are plotted in Figure 8 with the square cavity current $I_{\rm SQ}$ = 10 mA. In Figure 8(a), bare WGM lasing modes are observed with a mode wavelength interval of 22.3 nm

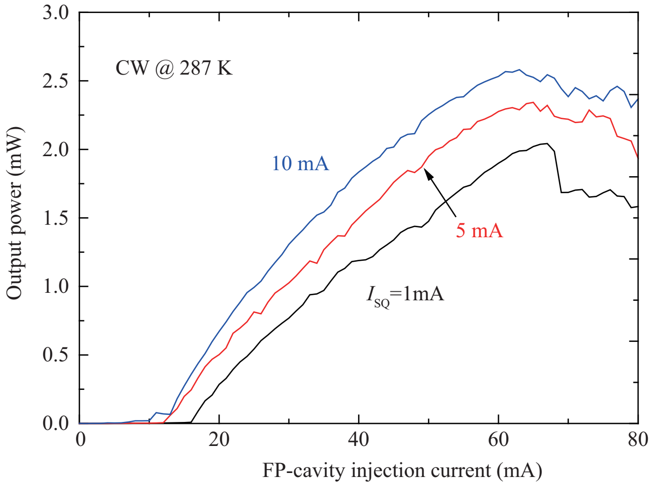

Figure 7 (Color online) Output powers coupled into a single mode fiber versus $I_{\rm FP}$ for a hybrid cavity laser with a square side length a = 10 μm, and the FP cavity width d = 1.5 μm and length L = 300 μm, at the square cavity injection current $I_{\rm SQ}$= 1, 5 and 10 mA, respectively.

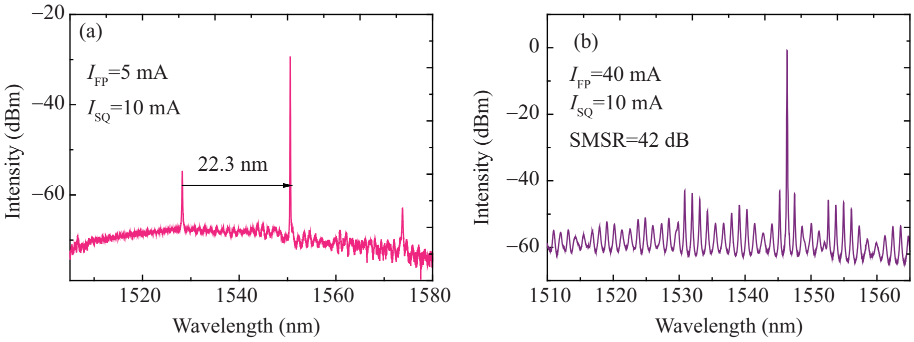

Figure 8 (Color online) Lasing spectra at the square cavity injection current 10 mA and FP cavity injection current of (a) 5 mA and (b) 40 mA for the hybrid cavity laser with a square side length a = 10 μm, and the FP cavity width d = 1.5 μm and length L = 300 μm.

at $I_{\rm FP}$ = 5 mA, and single mode operation with a side mode suppression ratio of 42 dB is realized at 1546.4 nm at $I_{\rm FP}$ = 40 mA as shown in Figure 8(b). Stable single-mode lasing around 1546 nm is obtained as $I_{\rm SQ}$ increases from 3 to 15 mA and $I_{\rm FP}$ = 40 mA. Then lasing mode shifts faster with the increase of $I_{\rm SQ}$ due to heating effect is almost proportional to squared $I_{\rm SQ}$, and lasing mode jumps with a wavelength interval of the FP cavity longitudinal mode interval as shown in [13], which can be set to satisfy different channels of wavelength division multiplexing communication systems.

Clear anti-crossing mode coupling is observed for a HSRL with a = 15 μm, d = 2 μm, and L = 300 μm, with the lasing spectra map versus $I_{\rm FP}$ as shown in Figure 9 at $I_{\rm SQ}$ = 10 mA. When $I_{\rm FP}$ increases, the FP modes firstly move to shorter wavelengths due to the free carrier dispersion below threshold and subsequently shift to longer wavelengths because of heating effect. The corresponding mode wavelengths and Q factors are plotted in Figure 9(b) and (c) for coupled modes, with the Q factors deduced based on the full-width at the half-maximum of resonant peaks. Around mode anti-crossing coupling point, the Q factor of one hybrid mode reduces from 1.13×10^4 to 4.5×10^3 as $I_{\rm FP}$ is increased from 4 to 8 mA, but the Q factor of another hybrid mode increases from 1.5×10^3 to 1.0×10^4. The results indicate the mode Q factor enhancement due to the mode coupling clearly.

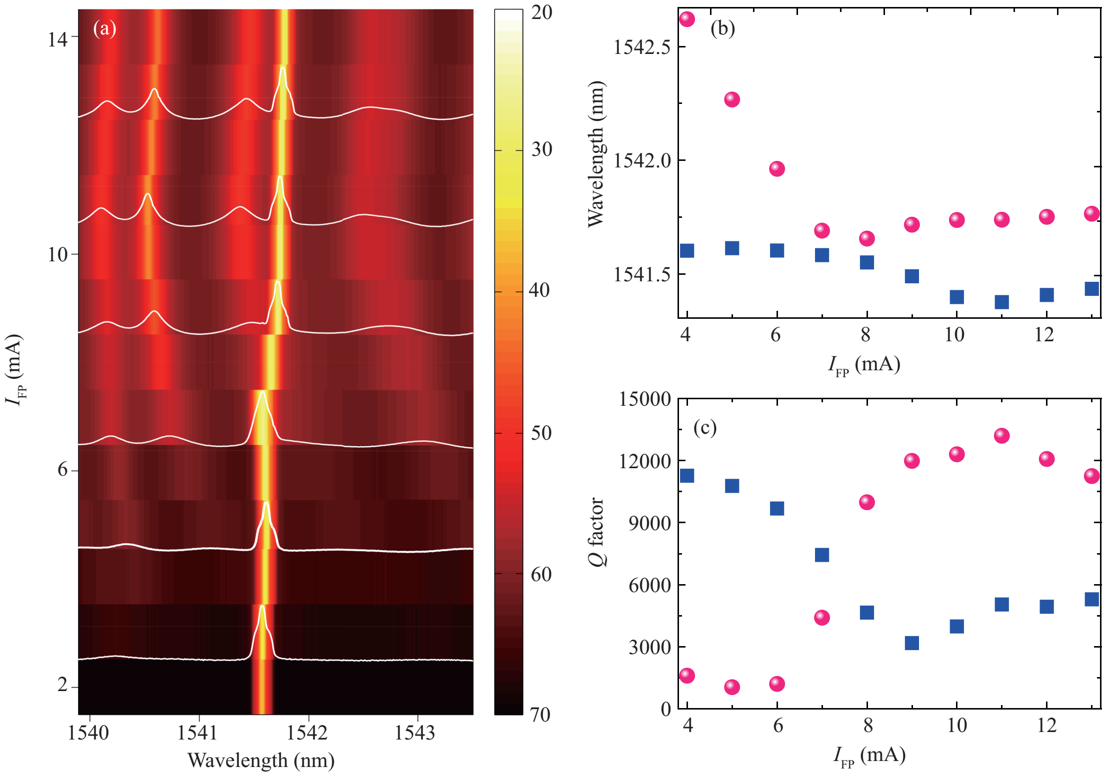

Figure 9 (Color online) (a) Lasing spectra map exhibits the mode coupling with the variation of FP cavity injection current at $I_{SQ} = 10$ mA, for a HSRL with $a = 15$ μm, $d = 2$ μm, and $L = 300$ μm. The white curves are the lasing spectra at $I_{FP} = 3$, 5, 7, 9, 11, and 13 mA, respectively. (b) Mode wavelengths and (c) Q factors for the hybrid modes as functions of I_{FP}.

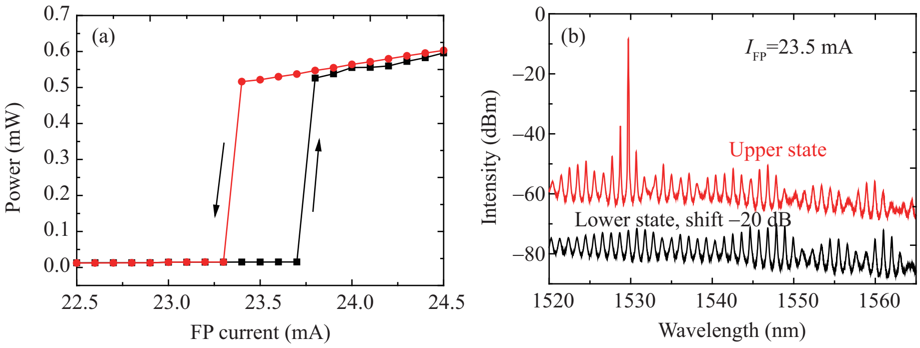

Figure 10 (Color online) (a) Single-mode fiber coupled output power versus I_{FP} of the first bistable region, and (b) the corresponding lasing spectra of the upper and lower states at $I_{FP} = 23.5$ mA, for a hybrid cavity laser with square side length $a = 15$ μm, $d = 1.5$ μm, and $L = 300$ μm as $I_{SQ} = 0$ and 287 K.

6 Optical bistable hybrid cavity laser with a square microcavity

Finally, we report optical bistability characteristics for a hybrid cavity laser with a square microcavity at side length $a = 15$ μm, and an FP cavity with $d = 1.5$ μm and $L = 300$ μm as in [26]. The laser was mounted on a heat sink and operated in continuous-wave current injection at 287 K. Output powers coupled into an SMF as functions of I_{FP} are measured by increasing and decreasing I_{FP}, respectively, at $I_{SQ} = 0$. Bistable hysteresis loops are observed around the threshold and between 43.5 to 51 mA, as shown in Figures 10(a) and 11(a). The bistable loop around threshold is caused by saturable absorption in the square cavity as the hybrid laser with a pentagon microcavity in Section 4.

The lasing spectra of the upper and lower states at $I_{FP} = 23.5$ mA and $I_{SQ}= 0$ are plotted in Fig-

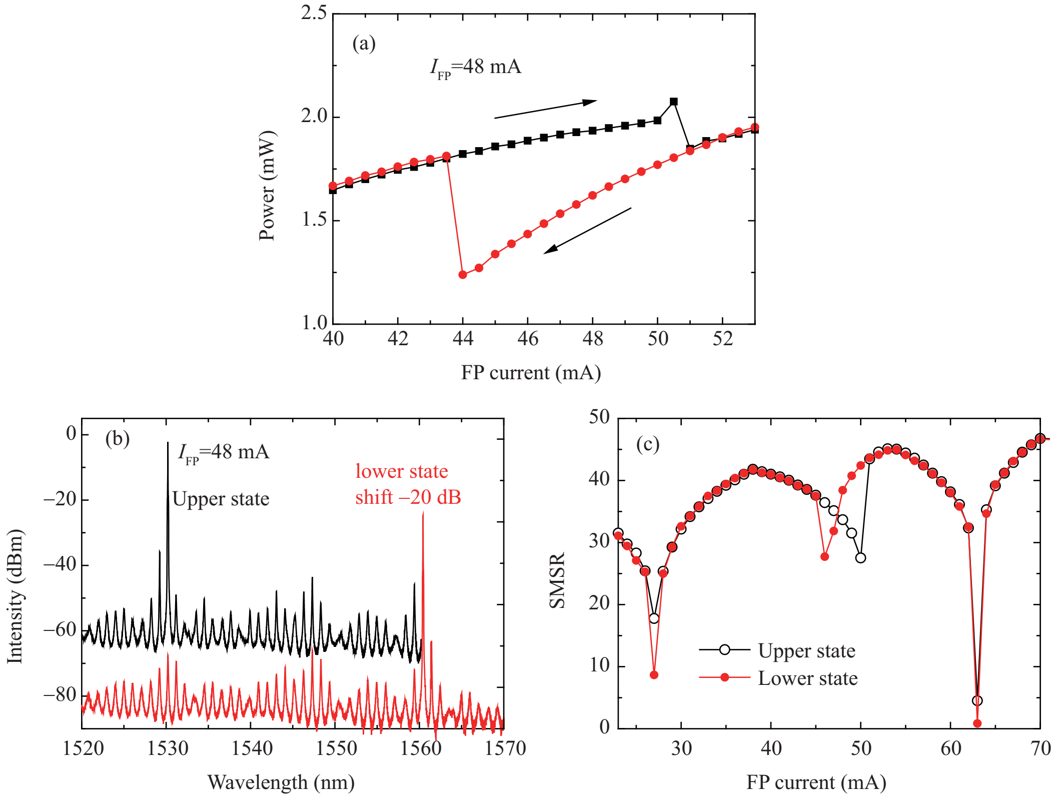

Figure 11 (Color online) (a) Single-mode fiber coupled output power versus $I_{\rm FP}$ of the second bistable region, (b) the corresponding lasing spectra of the upper and lower states at $I_{\rm FP}$ = 48 mA, and (c) the corresponding side-mode suppression ratio for the hybrid cavity laser with square side length a = 15 μm, d= 1.5 μm, and L = 300 μm as $I_{\rm SQ}$ = 0 and 287 K.

ure 10(b) with a lasing mode wavelength of 1530 nm in the upper state, which shows bistability switching between spontaneous emission state and lasing state. Furthermore, we present the lasing spectra in Figure 11(b) for the bistable states at $I_{\rm FP}$ = 48 mA and $I_{\rm SQ}$= 0, which shows lasing mode jumping from 1530.21 nm of the upper state to 1560.44 nm of the lower state. The lasing mode wavelength interval of 30.2 nm is corresponding to the high-Q mode wavelength interval 35.29 nm in Figure 3(a). The simulated mode interval is determined by a refractive index of 3.2, but the practical mode wavelength interval is smaller because it is determined by group index accounting the dispersive. The optical bistability around $I_{\rm FP}$ = 48 mA is mainly caused by mode competition. The SMSRs versus $I_{\rm FP}$ are plotted in Figure 11(c), which takes the highest value of 45 dB at $I_{\rm FP}$ = 53 mA and drops to 27 dB near the transition points of hybrid modes of different WGMs. In addition, the low SMSR values at 27 and 63 mA are caused by the transitions of mode couplings between WGMs with different FP modes with a wavelength interval of 0.9 nm, due to a faster temperature rise in FP cavity in contrast to the square cavity.

Based on the output powers of the two lasing modes, we can realize optical memory switched by injecting optical pulse at different lasing mode wavelengths. For bistable states at λ_A = 1530.21 nm and λ_B = 1560.44 nm, the hybrid cavity laser can keep lasing at λ_A or λ_B over long time after switching in the experiment. The all-optical flip-flop operations are demonstrated using set/reset optical pulses with the width of 100 ps at λ_A and λ_B as shown in Figure 12(a). Under the optical pulses, the output optical powers at the wavelength channels of λ_A and λ_B are shown in Figure 12(b) and (c), respectively, with on/off contrast ratio of about 8 dB. Subtracting the coupling loss, we estimate the injected peak powers of 27 μW and 142 μW for λ_B and λ_A states. The corresponding switching pulse energies are 2.7 fJ and 14.2 fJ, and the rising and falling times are 165 ps and 60 ps for λ_B dominant state, and 177 ps and 69 ps for λ_A dominant state, respectively.

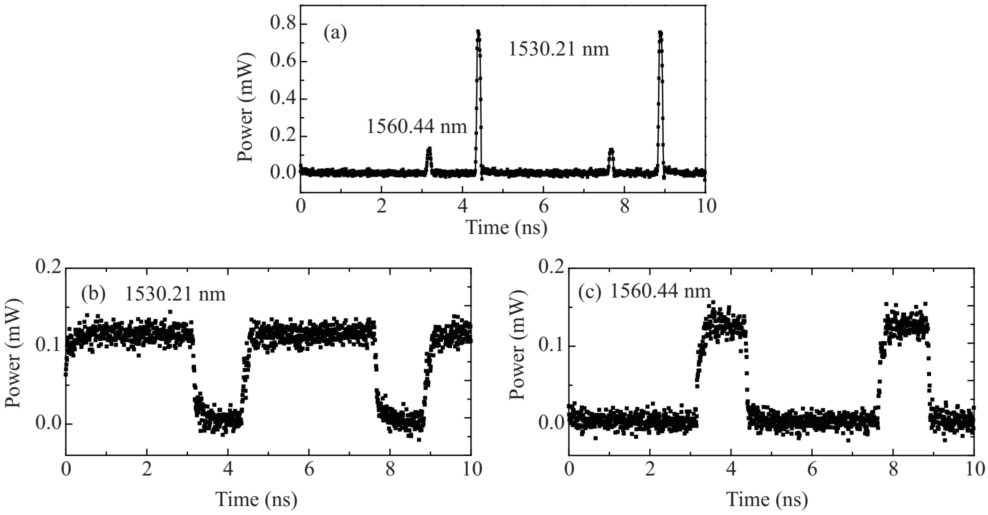

Figure 12 Oscilloscope traces showing the dynamic all-optical flip-flop operation. (a) Input trigger optical pulses for the set/reset signals with the pulse width of 100 ps. Output optical signals at (b) 1530.21 nm and (c) 1560.44 nm under the trigger pulses for the hybrid cavity laser with square side length $a = 15$ μm, $d= 1.5$ μm, and $L = 300$ μm at $I_{\rm SQ} = 0$, $I_{\rm FP}=$ 48 mA, and 287 K.

7 Conclusion

In conclusion, we report single mode operation and optical bistability behaviors for hybrid cavity lasers composed of an FP cavity and a WGM microcavity. The coupled modes between WGMs and FP modes with enhanced mode Q factor are numerically and experimentally demonstrated, which have a wavelength interval as that of the longitudinal mode of a microcavity. Stable single mode operations are realized for hybrid cavity lasers. Furthermore, we can have high output power and high coupling efficiency to a single mode fiber for hybrid cavity lasers, although the simulated transverse mode field pattern inside the FP cavity is also a hybrid mode instead of the fundamental mode. In addition to realize single mode laser, hybrid cavity lasers can reach optical bistability, as the microcavity is unbiased, due to saturable absorption in the microcavity section and mode competition, respectively. Ultra-fast all-optical flip-flop operations are demonstrated using the mode competition optical bistability.

Compared to traditional cleaved coupled-cavity lasers, the interface between microcavity and FP cavity is like a soft transition area for the hybrid cavity lasers, which results in more stable hybrid cavity lasers. The high Q coupled modes have strong mode field distribution in microcavity section. The experimental results show that the hybrid cavity lasers can be a robust single mode laser with the variation of injection currents, which is important for practical application. The hybrid cavity laser is a potential single mode light source for photonic integrated circuits, and optical bistability and all-optical flip-flop makes it useful for optical signal processing. Based on the planar technology process, we expect that cascaded hybrid cavity lasers can be fabricated for signal processing.

Acknowledgements This work was supported by National Natural Science Foundation of China (Grant Nos. 61235004, 61527823, 61376048).

References

1 McCall S L, Levi A F J, Slusher R E, et al. Whispering-gallery mode microdisk lasers. Appl Phys Lett, 1992, 60: 289–291

2 Choi S J, Djordjev K, Sang J C K, et al. Microdisk lasers vertically coupled to output waveguides. IEEE Photon Technol Lett, 2003, 15: 1330–1332

3 Audet R, Belkin M A, Fan J A, et al. Single-mode laser action in quantum cascade lasers with spiral-shaped chaotic resonators. Appl Phys Lett, 2007, 91: 131106

4 Song Q H, Ge L, Stone A D, et al. Directional laser emission from a wavelength-scale chaotic microcavity. Phys Rev

Lett, 2010, 105: 103902

5 Jiang X F, Xiao Y F, Zou C L, et al. Highly unidirectional emission and ultralow-threshold lasing from on-chip ultrahigh-Q microcavities. Adv Mater, 2012, 24: 260–264

6 Guo W-H, Huang Y-Z, Lu Q-Y, et al. Modes in square resonators. IEEE J Quantum Electron, 2003, 39: 1563–1566

7 Huang Y Z, Che K J, Yang Y D, et al. Directional emission InP/GaInAsP square-resonator microlasers. Opt Lett, 2008, 33: 2170–2172

8 Huang Y Z, Lü X M, Lin J D, et al. Output characteristics of square and circular resonator microlasers connected with two output waveguides. Sci China Technol Sci, 2013, 56: 538–542

9 Long H, Huang Y Z, Yang Y D, et al. Mode characteristics of unidirectional emission AlGaInAsInP square resonator microlasers. IEEE J Quantum Electron, 2014, 50: 981–989

10 Long H, Huang Y Z, Yang Y D, et al. Mode and modulation characteristics for microsquare lasers with a vertex output waveguide. Sci China-Phys Mech Astron, 2015, 58: 114205

11 Ma X W, Huang Y Z, Yang Y D, et al. Mode coupling in hybrid square-rectangular lasers for single mode operation. Appl Phys Lett, 2016, 109: 071102

12 Ma X W, Huang Y Z, Yang Y D, et al. Mode and lasing characteristics for hybrid square-rectangular lasers. IEEE J Sel Top Quantum Electron, 2017, 23: 1500409

13 Huang Y Z, Ma X W, Yang Y D, et al. Lasing characteristics of integrated lasers with whispering-gallery mode microresonator. In: Proceedings of Society of Photo-Optical Instrumentation Engineers (SPIE), San Francisco, 2016. 9751: 97510J

14 Tsang W T, Olsson N A, Logan R A. High-speed direct single-frequency modulation with large tuning rate and frequency excursion in cleaved-coupled-cavity semiconductor lasers. Appl Phys Lett, 1983, 42: 650–652

15 Coldren L A. Monolithic tunable diode lasers. IEEE J Sel Top Quantum Electron, 2000, 6: 988–999

16 He J J, Liu D. Wavelength switchable semiconductor laser using half-wave V-coupled cavities. Opt Expr, 2008, 16: 3896–3911

17 Shang L, Liu L, Xu L. Single-frequency coupled asymmetric microcavity laser. Opt Lett, 2008, 33: 1150–1152

18 D'Agostino D, Lenstra D, Ambrosius H P M M, et al. Coupled cavity laser based on anti-resonant imaging via multimode interference. Opt Lett, 2015, 40: 653–656

19 Li X, Zhu Z, Xi Y, et al. Single-mode Fabry-Perot laser with deeply etched slanted double trenches. Appl Phys Lett, 2015, 107: 091108

20 Tanaka Y, Upham J, Nagashima T, et al. Dynamic control of the Q-factor in a photonic crystal nanocavity. Nat Mater, 2007, 6: 862–865

21 Hughes S. Coupled-cavity QED using planar photonic crystals. Phys Rev Lett, 2007, 98: 083603

22 Tanabe T, Notomi M, Taniyama H, et al. Dynamic release of trapped light from an ultrahigh-Q nanocavity via adiabatic frequency tuning. Phys Rev Lett, 2009, 102: 043907

23 Sato Y, Tanaka Y, Upham J, et al. Strong coupling between distant photonic nanocavities and its dynamic control. Nat Photon, 2011, 6: 5661

24 Dündar M A, Voorbraak J A M, Nötzel R, et al. Multimodal strong coupling of photonic crystal cavities of dissimilar size. Appl Phys Lett, 2012, 100: 081107

25 Jin C Y, Johne R, Swinkels M Y, et al. Ultrafast non-local control of spontaneous emission. Nat Nanotech, 2014, 9: 886–890

26 Ma X W, Huang Y Z, Yang Y D, et al. All-optical flip-flop based on hybrid square-rectangular bistable lasers. Opt Lett, 2017, 42: 2291–2294

27 Johnson J E, Tang C L, Grande W J. Optical flip-flop based on two-mode intensity bistability in a cross-coupled bistable laser diode. Appl Phys Lett, 1993, 63: 3273–3275

28 Kawaguchi H. Bistable laser diodes and their applications: state of the art. IEEE J Sel Top Quantum Electron, 1997, 3: 1254–1270

29 Saitoh E, Miyajima H, Yamaoka T, et al. Current-induced resonance and mass determination of a single magnetic domain wall. Nature, 2004, 432: 203–206

30 Takenaka M, Raburn M, Nakano Y. All-optical flip-flop multimode interference bistable laser diode. IEEE Photon Technol Lett, 2005, 17: 968–970

31 Huybrechts K, Morthier G, Baets R. Fast all-optical flip-flop based on a single distributed feedback laser diode. Opt Expr, 2008, 16: 11405–11410

32 Liu L, Kumar R, Huybrechts K, et al. An ultra-small, low-power, all-optical flip-flop memory on a silicon chip. Nat Photon, 2010, 4: 182–187

33 Wu Y, Zhu Y, Liao X, et al. All-optical flip-flop operation based on bistability in V-cavity laser. Opt Expr, 2016, 24: 12507–12514

34 Fitsios D, Alexoudi T, Bazin A, et al. Ultra-compact III-V-on-Si photonic crystal memory for flip-flop operation at 5 Gb/s. Opt Expr, 2016, 24: 4270–4277

35 Alexoudi T, Fitsios D, Bazin A, et al. III-V-on-Si photonic crystal nanocavity laser technology for optical static random access memories. IEEE J Sel Top Quantum Electron, 2016, 22: 4901410

36 Mori T, Yamayoshi Y, Kawaguchi H. Low-switching-energy and high-repetition-frequency all-optical flip-flop operations of a polarization bistable vertical-cavity surface-emitting laser. Appl Phys Lett, 2006, 88: 101102

37 Katayama T, Ooi T, Kawaguchi H. Experimental demonstration of multi-bit optical buffer memory using 1.55-μm polarization bistable vertical-cavity surface-emitting lasers. IEEE J Quantum Electron, 2009, 45: 1495–1504

38 Alharthi S S, Hurtado A, Korpijarvi V M, et al. Circular polarization switching and bistability in an optically injected 1300 nm spin-vertical cavity surface emitting laser. Appl Phys Lett, 2015, 106: 021117

39 Guo W-H, Li W-J, Huang Y-Z. Computation of resonant frequencies and quality factors of cavities by FDTD technique and Pade approximation. IEEE Microw Wireless Compon Lett, 2001, 11: 223–225

40 Yang Y D, Wang S J, Huang Y Z. Investigation of mode coupling in a microdisk resonator for realizing directional emission. Opt Expr, 2009, 17: 23010–23015

41 Harder C, Lau K Y, Yariv A. Bistability and pulsations in CW semiconductor lasers with a controlled amount of saturable absorption. Appl Phys Lett, 1981, 39: 382–384

42 Li J, Wang Q. A common-cavity two-section InGaAsP/InP bistable laser with a low optical switching power. Opt Commun, 1991, 83: 71–75